Hydrogen evolution enhancement of ultra-low loading, size-selected molybdenum sulfide nanoclusters by sulfur enrichment

Escalera-López, Daniel; Niu, Yubiao; Park, Sung Jin; Isaacs, Mark; Wilson, Karen; Palmer, Richard E.; Rees, Neil V.

[Link to publication on Research at Birmingham portal](#)

Hydrogen evolution enhancement of ultra-low loading, size-selected molybdenum sulfide nanoclusters by sulfur enrichment

Daniel Escalera-López[a,b,1], Yubiao Niu[b,c,1], Sung Jin Park[b,d], Mark Isaacs[e], Karen Wilson[e,f], Richard E. Palmer[c], Neil V. Rees[a,*]

[a] Centre for Hydrogen and Fuel Cell Research, School of Chemical Engineering, University of Birmingham, Birmingham, B15 2TT, UK
[b] Nanoscale Physics Research Laboratory, School of Physics and Astronomy, University of Birmingham, Birmingham, B15 2TT, UK
[c] College of Engineering, Swansea University, Bay Campus, Fabian Way, Swansea, SA1 8EN, UK
[d] Key Laboratory of Materials Modification by Laser, Ion and Electron Beams, Department of Physics, Dalian University of Technology, Dalian, 116024, China
[e] European Bioenergy Research Institute, Aston University, Birmingham, B4 7ET, UK
[f] School of Science, RMIT University, 124 La Trobe Street, Melbourne, VIC, 3000, Australia

ARTICLE INFO

ABSTRACT

Size-selected molybdenum sulfide (MoS_x) nanoclusters obtained by magnetron sputtering and gas condensation on glassy carbon substrates are typically sulfur-deficient ($x = 1.6 \pm 0.1$), which limits their crystallinity and electrocatalytic properties. Here we demonstrate that a sulfur-enriching method, comprising sulfur evaporation and cluster annealing under vacuum conditions, significantly enhances their activity towards the hydrogen evolution reaction (HER). The S-richness ($x = 4.9 \pm 0.1$) and extended crystalline order obtained in the sulfur-treated MoS_x nanoclusters lead to consistent 200 mV shifts to lower HER onset potentials, along with two-fold and more-than 30-fold increases in turnover frequency and exchange current density values respectively. The high mass activities ($\sim 111 \, \text{mA mg}^{-1}$ @ 400 mV) obtained at ultra-low loadings ($\sim 100 \, \text{ng cm}^{-2}$, 5% surface coverage) are comparable to the best reported MoS_2 catalysts in the literature.

1. Introduction

The interest in the hydrogen economy as a potential candidate to replace the current fossil fuel-based energy system [1] has motivated extensive research on environmentally-friendly hydrogen production methods. The hydrogen evolution reaction (HER) taking place at a water electrolyser cathode is a scalable yet energy-efficient route [2] which demands earth-abundant catalysts to be commercially viable. Among them, transition metal dichalcogenides (TMDs) and in particular molybdenum disulfide (MoS_2) have stood out in the past decade [3,4]. Their layered structure, analogous to that of graphene, also implies anisotropic properties: only the metallic 1 T phase sites located at the Mo-edge planes of naturally occurring MoS_2 are active for the HER [5,6], whereas the 2 H semiconducting basal planes are almost inactive if no defects are present [7–9]. Several strategies have proven to maximize MoS_2 HER activities: [10] triggering the $2H \rightarrow 1T$ phase transition in basal planes by chemical intercalation [11–13] or stress/strain effects; [14,15] basal plane activation by incorporation of transition metals [16–20] or other chalcogenides; [21,22] and the fabrication of MoS_x nanostructures which are defect-rich [23–30] or have

additional S vacancies [31–36]. However, the in-operando proven role of S atoms as the HER active sites [37] indicates that sulfur-rich MoS_{2+x} materials should also present high HER activities [38–41]. Our recently reported size-selected MoS_x nanoclusters, obtained by magnetron sputtering and gas condensation [42], were demonstrated to be sulfur-deficient ($x = 1.6 \pm 0.1$) with low crystallinities. In this article we have evaluated the influence of sulfur content in the HER catalysis of MoS_2 materials through use of an in vacuo sulfur addition treatment previously developed for freshly deposited, sulfur-deficient $(MoS_x)_{1000}$ nanoclusters [43]. We demonstrate that sulfur evaporation (5 min) followed by annealing treatment (7 min, $215 \pm 5\,°C$) incorporates S in the MoS_x nanocluster structure ($x = 4.9 \pm 0.1$), by reducing oxygen-containing Mo surface species and converting the amorphous S_2^{2-} moieties to crystalline S^{2-} sites, which also extends the crystalline order. A consistent 200 mV shift to lower HER overpotential, along with a two-fold increased turnover frequency and more-than 30-fold increase of exchange current density values proves the beneficial role of higher S surface content and crystallinities in the $(MoS_x)_{1000}$ nanoclusters HER catalysis.
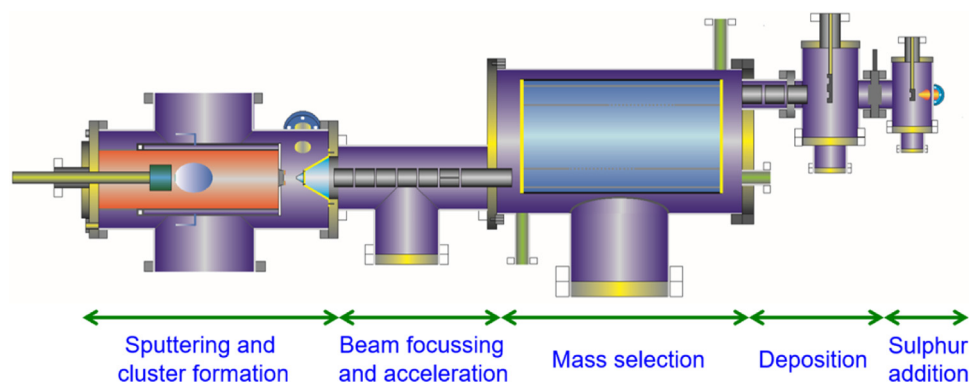
Fig. 1. Cluster beam source schematic. It consists of five sections: magnetron sputtering, ion optics, mass filter, cluster deposition and cluster post-treatment.

2. Experimental

2.1. $(MoS_x)_{1000}$ nanoclusters deposition and high-angle annular dark-field scanning transmission electron microscopy (HAADF-STEM) imaging

Size-selected MoS_2 nanoclusters were produced using a DC magnetron sputtering and gas condensation cluster beam source as shown in Fig. 1 from a 2-inch sputtering MoS_2 target (PI-KEM, 99.9% purity) [44]. The positively charged clusters were accelerated with ion optical electrostatic lenses and then size-selected with a lateral time-of-flight mass filter [45]. A mass of 160,000 amu, corresponding to 1000 MoS_2 units (designated as $(MoS_2)_{1000}$), was selected for depositing onto an amorphous carbon coated TEM grids (Agar Scientific, 200 Mesh Cu) and onto glassy carbon (GC) stubs (5 mm × 5 mm x 3 mm, mirror finish). The loading of the TEM grid samples was approx. 5% projected surface area coverage (i.e., approx. 5% of the surface covered by clusters), while the loadings of the GC samples were 5%, 10% and 20% projected surface area. The clusters were deposited onto amorphous carbon covered TEM grids and GC stubs with an impact energy of 1.0 eV and 1.5 eV per MoS_2 unit, respectively. Sulfur addition was conducted in a sulfur atmosphere created by evaporating sulfur using a home-built in-situ thermal evaporator (5 min). Annealing (7 min, 215 ± 5 °C) was performed with an electron beam bombardment heating stage. The temperature was monitored using a pyrometer (IMPAC Pyrometer, IPE 140). Scanning transmission electron microscopy (STEM) images were acquired with a 200 kV spherical aberration-corrected STEM (JEOL 2100 F) in the high-angle annular dark-field (HAADF) mode [46,47].

2.2. Physical characterization of $(MoS_x)_{1000}$ nanoclusters: X-ray photoelectron spectroscopy (XPS)

XPS spectra were recorded using a Kratos Axis SUPRA fitted with a monochromated aluminium source (Al Kα, 1486.69 eV) and a charge neutraliser. Samples were mounted on silicon wafers by use of silver epoxy, and affixed to a sample bar using carbon tape. Wide scans were recorded using pass energies of 160 eV and high-resolution scans were recorded using pass energies of 20 eV and an analysis area of 30 μm². All scans were recorded at $< 5 \times 10^{-9}$ Torr using an emission current of 15 mA. All high-resolution spectra were corrected to the adventitious C 1 s peak at 284.6 eV, and deconvoluted using the CasaXPS 2.3.18 software, applying a Shirley background correction before individual peak deconvolution. $Mo^aO_bS_c$ is used to refer to the molybdenum oxysulfide species: the superscript [a] represents the oxidation state of Mo, whilst the subscripts [b] and [c] the stoichiometry of O and S atoms in the specific oxysulfide.

2.3. Electrochemical characterization

All electrochemical measurements were performed in a conventional 3-electrode electrochemical setup comprising a thermostatted two-compartment cell (295 ± 2 K), the first compartment containing both a saturated calomel reference electrode (SCE, BAS Inc., Japan) and 5 mm diameter, 3 mm thick glassy carbon working electrodes (GC) type 2 stubs (Alfa Aesar, U.K.) modified with as deposited or sulfur evaporated and annealed $(MoS_x)_{1000}$ nanoclusters; and a second compartment containing a bright Pt mesh counter electrode (Alfa Aesar, U.K.). All experiments were conducted using a PC-controlled PGSTAT128N potentiostat (Metrohm Autolab B.V, Netherlands). GC samples were polished to until a mirror finish was achieved by use of decreasing size diamond (45–3 μm) and alumina slurries (1–0.05 μm) on a Buehler MetaServ 250 automatic polisher using Trident/Microcloth polishing pads. All GC samples were immediately tested after nanocluster modification, being transported to the electrochemical cell in a N_2-saturated sealed container to avoid exposure to air. The nanocluster-modified GC stubs were embedded in a E4TQ ChangeDisk RDE Tip and electrically connected to a E4 Series Rotating Shaft and a Modulated Speed Rotator (Pine Research Instrumentation, USA). No rotation was applied during any electrochemical experiment.

A 2 mM $HClO_4$ (ACS ≥ 70%, Sigma-Aldrich), 0.1 M $NaClO_4$ (ACS ≥ 98%, Sigma-Aldrich) solution (pH 2.7) was used in all experiments, freshly prepared with ultrapure water (Millipore Mili-Q Direct 8, resistivity not less than 18.2 MΩ cm). This fully supported, non-coordinating anion-containing, low proton concentration electrolyte was chosen in contrast to the more commonly reported high proton concentration electrolytes in hydrogen evolution experiments (0.5 M H_2SO_4, pH ≈ 0.3; 0.1 M $HClO_4$, pH ≈ 1) as previous experiments on $(MoS_x)_y$ nanoclusters yielded more reproducible electrochemical results, enabling accurate elucidation of the HER reaction kinetic parameters. Acidic electrolytes with lack of a supporting electrolyte (in our case 0.1 M $NaClO_4$) are reported to distort any kinetic analysis due to migration effects of the electroactive species [48].

Nanocluster-modified GC electrodes were preconditioned prior to HER experiments with 10 cycles from −0.045 to −1.645 V (vs. SCE) at a voltage scan rate of 50 mVs^{-1} to obtain a stabilized performance. HER electrocatalysis measurements were then recorded at a range of voltage scan rates from 2 to 1200 mVs^{-1}, and electrochemical impedance spectroscopy measurements (EIS) were acquired in the −0.1 to −1.4 V vs. SCE with 100 mV steps, using a frequency range of 10^{-1} to 10^5 Hz (voltage amplitude = 10 mV) to apply the *iR* compensation correction on all HER voltammograms. All HER potentials reported are corrected versus the normal hydrogen electrode (NHE) using the Nernstian shift correction ($E_{NHE} = 0.242$ V + 0.059 pH). The electrochemical cell was vigorously purged with N_2 prior to any electrochemical experiment (Oxygen-free grade, BOC Gases plc), and a positive N_2 pressure was maintained during experiments. All electrochemical glassware was cleaned overnight by use of a dilute $KMnO_4$ (ACS ≥ 99%, Sigma-Aldrich) solution in concentrated H_2SO_4 (> 95% analytical grade, Fisher Scientific) followed by rinsing with
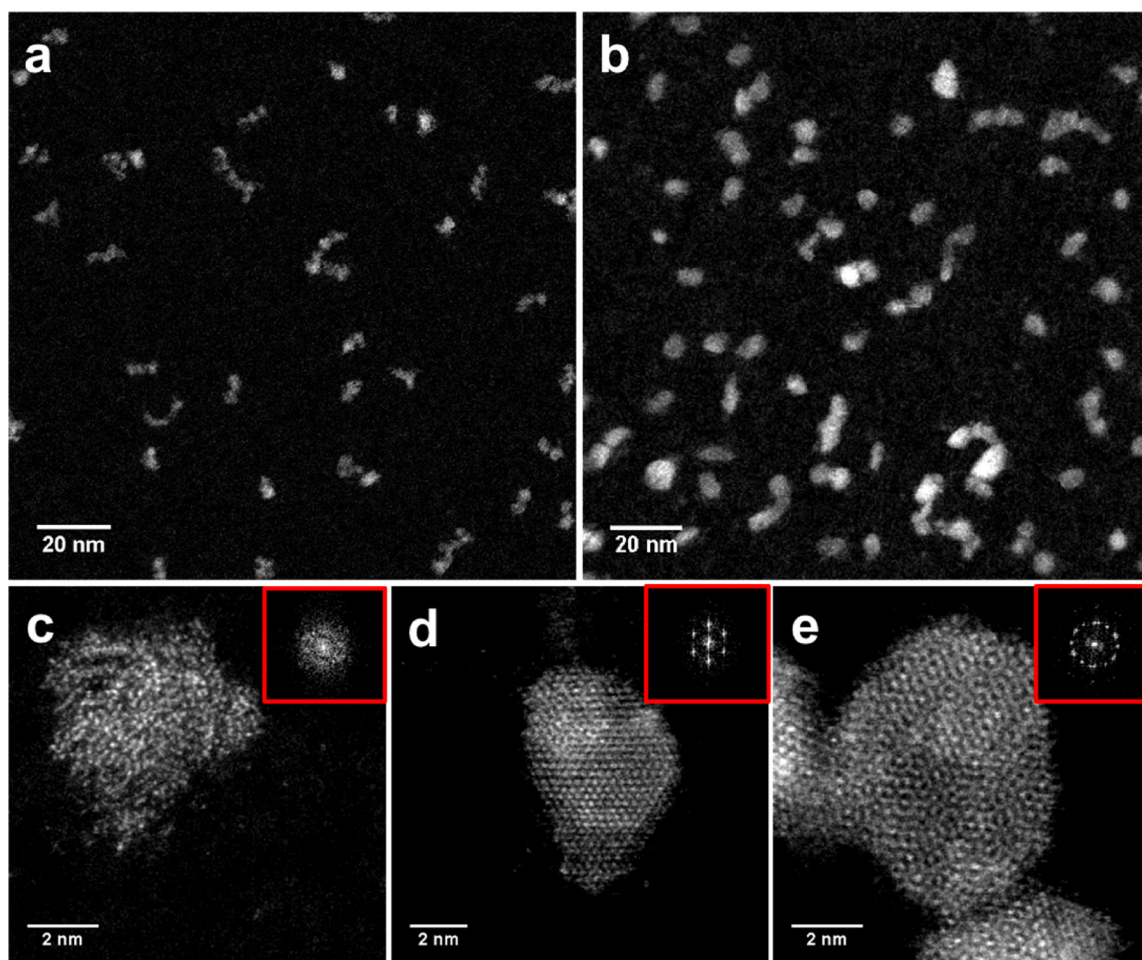
Fig. 2. STEM images of as-deposited size-selected $(MoS_x)_{1000}$ nanoclusters shown at a) low and c) high magnification, and STEM images of $(MoS_x)_{1000}$ nanoclusters after sulfur evaporation and annealing at b) low magnification and d, e) high magnification. The insets shown in c, d and e are the FFT patterns of corresponding clusters.

ultrapure water.

3. Results and discussion

3.1. Physical characterization of size-selected $(MoS_x)_{1000}$ nanoclusters: HAADF-STEM imaging and XPS

Fig. 2 shows the aberration-corrected HAADF-STEM images of $(MoS_x)_{1000}$ nanoclusters (selected mass at cluster source, 160,000 amu, equivalent to 1000 MoS_2 units per cluster) at 5% projected surface area coverage after deposition on amorphous carbon covered TEM grids. For cluster source schematic and further deposition parameters, see Fig. 1. Fig. 2a and b are acquired at low magnification before and after sulfur evaporation and annealing, respectively. The as-deposited MoS_x clusters are rather irregular with poorly ordered structures, and a mean diameter of 5.5 nm is given based on the projected surface area from our previous study [43]. The STEM image of as-deposited MoS_x cluster at a higher magnification (Fig. 2c), together with its FFT pattern (inset), show the amorphous feature of the cluster and confirm the absence of extended crystalline order. The clusters have an uneven layered structure revealed by the HAADF intensity line profile, which agrees with previous first-principle simulation studies [49]. Compared with the as-deposited clusters, the sulfurised clusters become larger with a mean diameter of 6.0 nm. This is due to the morphological reconstruction of MoS_x clusters with the added sulfur. In contrast to the as-deposited clusters, the sulfurised clusters shown in Fig. 2d and e present rather crystalline structures, which can also be confirmed by their FFT

patterns (inset). The sulfurised clusters retain the layered structure with 3–4 layers-thick. The Moirépattern shown in Fig. 2e indicates a misorientation between layers, which can be commonly found in the sulfurised clusters with 3 or more layers. Given that sulfur is long known to sublime at temperatures well below 100 °C [50,51], we can conclude that the crystalline structures come from the chemical bond between the added sulfur and the clusters, and that the structural modification into crystalline clusters mainly takes place within the 2D layers.

XPS measurements were acquired from molybdenum sulfide clusters deposited onto amorphous carbon TEM grids to investigate the degree of sulfur incorporation. The high-resolution Mo 3d and S 2p spectra of the as-deposited molybdenum sulfide nanoclusters reveal a complex surface composition (see Fig. 3a). The Mo spectra (Fig. 3, top row) could not be solely deconvoluted into the Mo^{4+} $3d_{5/2:3/2}$ spin-orbit doublet characteristic of MoS_2 materials (binding energies of ~ 229.8 and ~ 232.9 eV, respectively). Two additional doublets were needed, ascribed to $Mo^aO_bS_c$ (~ 231.5 and ~ 234.6 eV, see Experimental for $Mo^aO_bS_c$ definition) and Mo^{6+} (~ 233.1 and ~ 236.2 eV) oxidation states reported in molybdenum compounds such as molybdenum oxysulfides [52] and MoO_3 [53]. Analysis of the Mo^{4+}: $Mo^aO_bS_c$: Mo^{6+} relative percentages (at. %) from the XPS photoemission intensities yields a relative ratio of 53.8:25.2:21.0 at. %, corroborating the significant proportion of oxidized molybdenum species at the nanoclusters. The S spectra (Fig. 3, bottom row) were deconvoluted using two $2p_{3/2:1/2}$ spin-orbit doublets related to the S^{2-} (~ 161.3 and ~ 162.5 eV) and S_2^{2-} (~ 162.6 and ~ 163.8 eV) oxidation states consistently reported for amorphous MoS_x thin films and nanoparticles
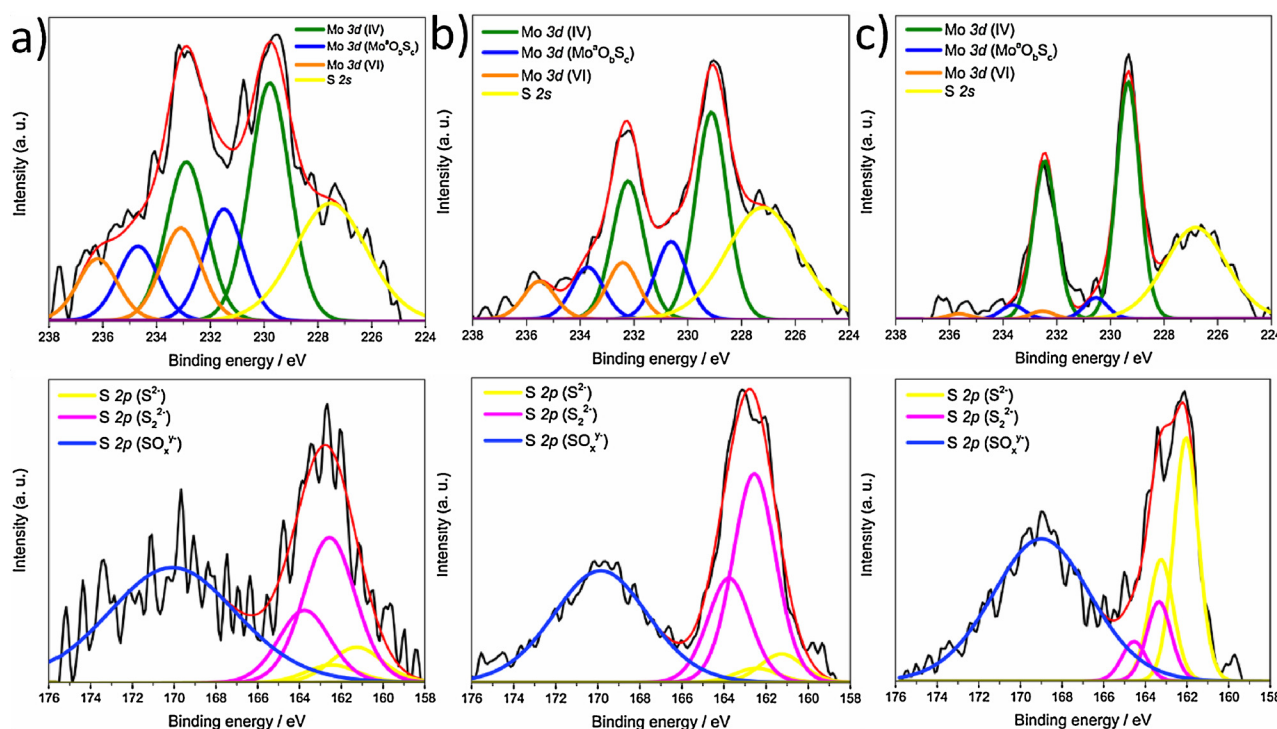
Fig. 3. High-resolution Mo 3d (top) and S 2p (bottom) XPS spectra of a) as-deposited $(MoS_x)_{1000}$ nanoclusters, b) sulfurised, non-annealed $(MoS_x)_{1000}$ nanoclusters and c) sulfurised, annealed $(MoS_x)_{1000}$ nanoclusters. Labels: raw spectra (black), cumulative peak fit (red), Mo^{4+} $3d_{5/2:3/2}$ (green), $Mo^aO_bS_c$ $3d_{5/2:3/2}$ (blue), Mo^{6+} $3d_{5/2:3/2}$ (orange), S $2p_{3/2:1/2}$ (S^{2-}, yellow) and S $2p_{3/2:1/2}$ (S_2^{2-}, magenta) (For interpretation of the references to colour in this figure legend, the reader is referred to the web version of this article).

[54,55], yielding a S^{2-} / S_2^{2-} relative ratio of 20:80. The broad S signal centered at ca. 170 eV is ascribed to SO_x^{y-} species [56], The XPS intensity ratio between the S-containing Mo species (Mo^{4+}/$Mo^aO_bS_c$) and the S^{2-} / S_2^{2-} species yields a close-to-stoichiometric but still S-deficient ratio (1:1.9 ± 0.1), similar to that found in our previous investigations [42,57].

Likewise, high-resolution XPS spectra on the sulfur-evaporated and annealed $(MoS_x)_{1000}$ nanoclusters (Fig. 3c) reveal an almost total conversion of oxidized Mo species to Mo^{4+} (Mo^{4+}: $Mo^aO_bS_c$: Mo^{6+} at. % ratio of 88.9:8.0:3.1), as well as an effective S-enrichment, obtaining a Mo^{4+}/$Mo^aO_bS_c$: S^{2-} / S_2^{2-} ratio of 1: 4.9 ± 0.1. As for the S^{2-} / S_2^{2-} XPS intensity ratio, this is now 75:25. Further analysis of the sulfurised but non-annealed $(MoS_x)_{1000}$ nanoclusters sample (Fig. 3b) reveals that S incorporation onto the nanoclusters occurs at this stage to a certain extent (Mo^{4+}/$Mo^aO_bS_c$: S^{2-} / S_2^{2-} ratio of 1: 3.3 ± 0.1), but it leads neither to an effective depletion of oxygen-containing Mo species (Mo^{4+}: $Mo^aO_bS_c$: Mo^{6+} at. % ratio of 62.2:21.4:16.4), nor to full crystallization of the nanocluster structures [43]. Hence, it is concluded that the best methodology to produce S-enriched MoS_x nanoclusters with enhanced crystalline order is by the adoption of sequential sulfur evaporation and thermal annealing.

3.2. Electrocatalytic activity to the hydrogen evolution reaction: influence of sulfur enrichment

The hydrogen evolution activity of the as-prepared and sulfur-enriched $(MoS_x)_{1000}$ nanoclusters was evaluated in a 3-electrode electrochemical setup, by recording linear sweep voltammograms between 0 to −1.2 V (scan rate = 50 mV s^{-1}) in a 2 mM $HClO_4$/0.1 M $NaClO_4$ aqueous electrolyte (normalized vs. NHE and *iR* compensated, for further details, see Experimental). The low proton concentration in the electrolyte used ([H^+] ≈ 2 × 10^{-6} mol cm^{-3}, pH ≈ 2.7) is responsible for the diffusion decay peak profile in Fig. 4a and b, analogous to that found with our previously reported magnetron-sputtered nanoclusters.

[57,58] The as-prepared samples present onset potentials, |η_{onset}| for current densities of |j| = 0.05 mA cm^{-2}, of ca. 690 mV, which are ∼60 mV positively shifted compared to the recorded |η_{onset}| for bare glassy carbon. This confirms that even at ultra-low loadings MoS_2 effectively catalyzes the HER. The peak half-maximum overpotentials (|$\eta_{half\,max}$|) and current densities (|$j_{half\,max}$|) metrics previously used to describe the HER catalysis of magnetron-sputtered nanoclusters[57] are found to be ca. 810 mV and 0.31 mA cm^{-2}, respectively (see Table S1 ESI).

These are in good agreement with the results obtained for $(MoS_{0.9})_{300}$ nanoclusters, which presented a higher cluster loading (ca. 3.5 µg cm^{-2}) but equivalent surface coverage given the smaller cluster sizes (∼20%).[57] Interestingly, such ultra-low loadings of size-selected MoS_x nanoclusters used in the present work (5% coverage: ∼84 ng cm^{-2}, 10% coverage: ∼168 ng cm^{-2}, 20% coverage: ∼335 ng cm^{-2}) already present HER activities comparable to those of $(MoS_{0.9})_{300}$ nanoclusters with loadings higher by 1 order of magnitude. Despite both smaller dimensions (∼2.6 nm) and higher loadings, the S-deficient Mo:S ratio and cluster overlapping upon random surface landing can then explain the $(MoS_{0.9})_{300}$ nanoclusters' reported performance. After sulfur incorporation, all $(MoS_x)_{1000}$ nanoclusters exhibit remarkable improvements in their HER performance. A consistent 200 mV shift in the HER |$\eta_{half\,max}$| was found independently of the sample loading (see. Fig. 4a–b).

To gather further insight about the HER kinetics and electron transfer properties, Tafel slope analysis and electrochemical impedance spectroscopy (EIS) experiments were carried out before and after sulfur enrichment of $(MoS_x)_{1000}$ nanoclusters. Tafel plots of the cathodic linear sweep voltammograms (|η| vs. log|j_{geom}|, Fig. 4c) show Tafel slopes in the 143–154 mV dec^{-1} range for all $(MoS_x)_{1000}$ nanocluster samples irrespective of both loading and sulfur modification, similar values to the one found for bare GC (≈154 mV dec^{-1}). This indicates that the sulfurisation treatment does not modify the mechanism under which the HER operates: for slopes close to b ≈ 120 mV dec^{-1} this is
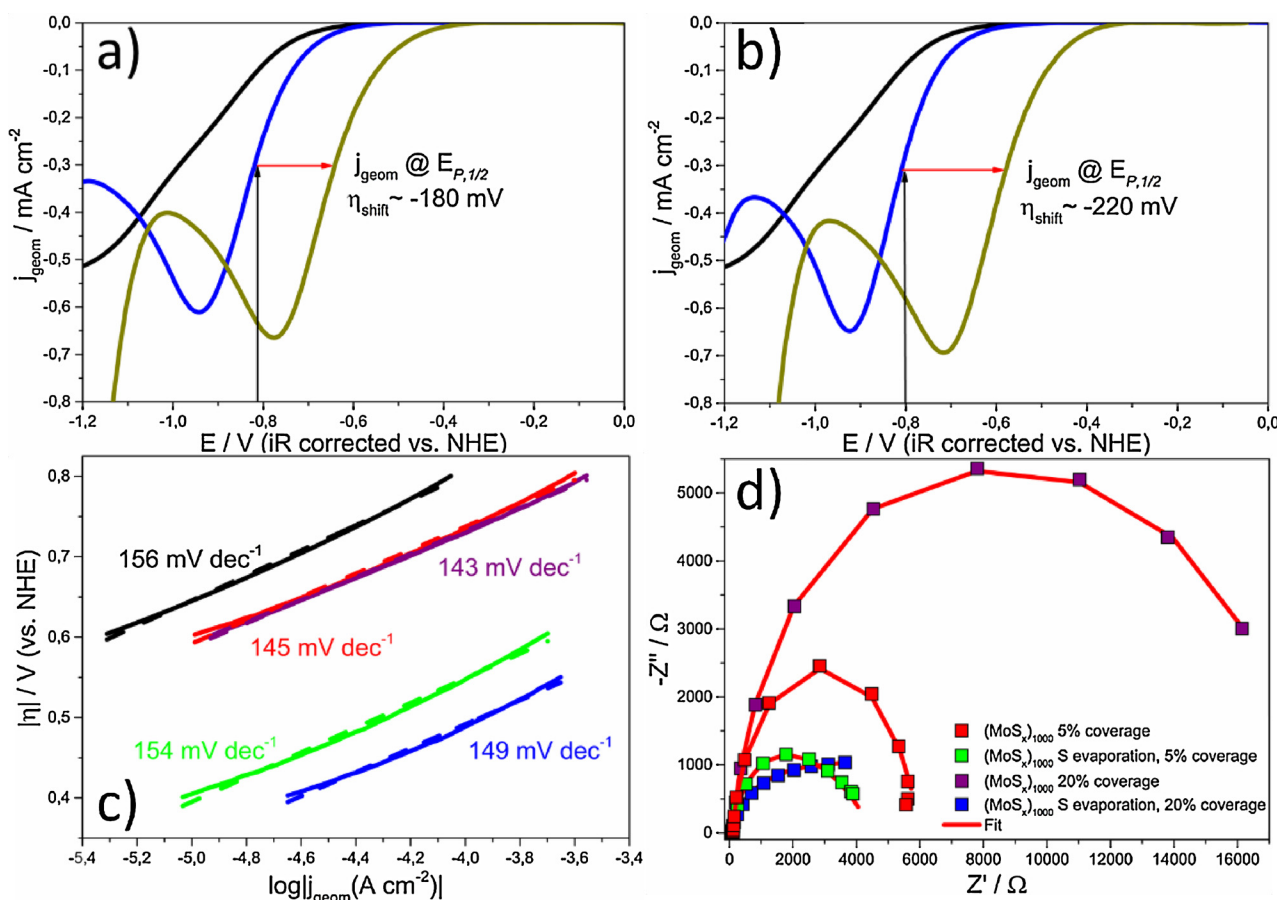
Fig. 4. a,b) Linear sweep voltammograms recorded at 5 mm diameter mirror-polished glassy carbon samples (black) modified with as-deposited $(MoS_x)_{1000}$ nanoclusters (blue) and sulfurised, annealed $(MoS_x)_{1000}$ nanoclusters (gold) at surface coverages of 5% (a) and 20% (b). Red arrows denote overpotential shift due to sulfurisation at $|j_{half\ max}|$. c) Tafel plots ($|\eta|$ vs. $\log|j_{geom}|$) of the different $(MoS_x)_{1000}$ nanoclusters plotted in a,b). Scan rate: 50 mV s^{-1}. d) Electrochemical impedance spectroscopy Nyquist spectra of samples in a,b) recorded at $\eta \sim -700$ mV vs. NHE. Labels in c,d): mirror-polished glassy carbon (black), as-deposited $(MoS_x)_{1000}$ nanoclusters at 5% (red) and 20% (purple) coverage, and surfurised and annealed $(MoS_x)_{1000}$ nanoclusters at 5% (green) and 20% (blue) coverage (For interpretation of the references to colour in this figure legend, the reader is referred to the web version of this article).

the Volmer mechanism, its rate-limiting step being the electroadsorption of monoatomic hydrogen [59]. Previous reports on amorphous MoS_x catalysts have reported Tafel slopes of b ≈ 40 mV dec^{-1} (Volmer-Heyrovsky rate-limiting step), significantly lower than the ones obtained for the as-deposited amorphous $(MoS_x)_{1000}$ nanoclusters. Two main factors are responsible for this: the electrolyte pH and the inherent morphology or the clusters. Recent investigations by Dubouis et al. on electrodeposited, amorphous MoS_x materials have shown that the HER mechanism (and consequently the Tafel slope) is pH-dependent: [60] for pH ≤ 1, the hydronium cation electroreduction governs the proton reduction with pH-independent Tafel slopes of b ≈ 40 mV dec^{-1}; at higher pH values the lower proton concentration leads to mass transport limitations which ultimately result in the proton electroadsorption (i.e. Volmer rate-limiting HER step, b ≈ 120 mV dec^{-1}) dominating the HER. Alternatively, the 40 mV dec^{-1} Tafel slopes reported on amorphous MoS_x are well known to arise from the $[Mo_3S_{13}]^{2-}$ cluster-based structure and the different sulfur moieties entailed [61,62]. The pH ≥ 1 used for our electrolyte along with the trigonal prismatic coordination as found in 2 H-MoS_2 for our size-selected MoS_x nanoclusters [42] support the ca. 143–154 mV dec^{-1} Tafel slopes obtained.

Electrochemical impedance spectroscopy (EIS) Nyquist plots were fitted with a simplified equivalent circuit model based on the recently-used linear transmission model [63,64] for amorphous/porous MoS_x structures (see Fig. S1 ESI for further details) [65,66]. Unlike the Randles circuit conventionally used to physically describe the HER on TMD materials, this circuit not only accounts for the charge transfer

resistance (R_{ct}), but also for the contact resistance between the nanoclusters and the glassy carbon electrode interface (R_c). Such information is of physical relevance given the layer-dependent HER catalysis of TMDs and their inherently high through-plane resistance [67–71]. At -1.1 V vs. SCE (~ -0.7 V vs. NHE), a significant decrease in all EIS resistance components was found after the combined treatment of sulfur evaporation plus annealing on the $(MoS_x)_{1000}$ nanoclusters (Fig. 4d, Table S2 ESI): R_{ct} (~ 1240 vs. $\sim 1180\ \Omega$, 5% coverage; ~ 6060 vs. $\sim 840\ \Omega$, 20% coverage), and R_c (~ 4640 vs. $\sim 3250\ \Omega$, 5% coverage; $\sim 12,420$ vs. $\sim 6820\ \Omega$, 20% coverage). We postulate the extended crystalline order of the sulfur-enriched nanocluster structure to be the governing factor.

This can be supported by both the FFT analysis of the nanoclusters imaged by HAADF-STEM and the high-resolution S 2p XPS results. The former shows, after sulfur incorporation, that the $(MoS_x)_{1000}$ nanocluster FFT pattern changes from a diffuse ring characteristic of highly amorphous materials to a well-defined set of diffraction spots ranging from single sets ascribed to aligned MoS_2 layers along the (100) plane (intralayer spacing: 0.25 nm) to dual sets related to misoriented stacking layer arrangements [43]. The high-resolution S 2p XPS data monitoring the S^{2-}/S_2^{2-} intensity ratio, which serves as a descriptor of the degree of MoS_x crystallinity, reveals an increased S^{2-} relative content after the sulfur evaporation treatment: 75:25 vs. the 20:80 found in pristine nanoclusters. Thus, the sulfur evaporation and annealing not only incorporates sulfur into the nanocluster structures but also converts the characteristic amorphous $MoS_x/MoS_3\ S_2^{2-}$ moieties

[41,55,72,73] to S^{2-} as found in crystalline MoS_2 [74]. From these findings we can conclude that the sulfur evaporation and subsequent annealing of $(MoS_x)_{1000}$ nanoclusters results in an overall improvement in their charge transfer properties. A previous report on polymorphic MoS_2 (a system which resembles the non-crystalline nature of our as-deposited nanoclusters) revealed that electron hopping only occurs between metallic 1T domains bounded by semiconducting 2H regions, and therefore is limited [75].

On a separate note, it is also noteworthy to explore which are the potential HER active sites in our MoS_x nanoclusters. For amorphous MoS_x, terminal S_2^{2-} [76], bridging S_2^{2-} [37] or unsaturated Mo^{IV} centers (i.e. S vacancies) [40] have been proposed as moieties responsible for hydrogen evolution, reaching no unambiguous consensus to date. For the as-prepared $(MoS_x)_{1000}$ nanoclusters, the presence of terminal/ bridging S_2^{2-} as found in our S 2p XPS spectra seems to indicate they might participate in the HER along with the well-established TMD unsaturated S^{2-} active sites [5,77]. In the case of our S-enriched $(MoS_x)_{1000}$ nanoclusters, the almost total conversion of the partially-oxidized $Mo^aO_bS_c$ and S_2^{2-} species to Mo^{4+} and S^{2-} as found in crystalline MoS_2 and subsequent HER enhancement lead us to believe that the main HER actives are the unsaturated S^{2-} moieties.

3.3. Evaluation of figures of merit and catalyst benchmarking

Further catalyst benchmarking by turnover frequency (TOF) and exchange current density (j_0) analysis also demonstrates the HER enhancement observed. For 5% surface coverage, as-deposited $(MoS_x)_{1000}$ nanoclusters present TOF $\approx 3.0\,H_2\,s^{-1}$ and $j_0 \approx 8.8 \times 10^{-10}\,A\,cm^{-2}$ at $|\eta_{half\,max}| = 825\,mV$, whereas for an equivalent $|\eta_{half\,max}|$ the sulfur-modified $(MoS_x)_{1000}$ nanoclusters sample exhibits TOF $\approx 6.1\,H_2\,s^{-1}$ and $j_0 \approx 2.8 \times 10^{-8}\,A\,cm^{-2}$. At 20% surface coverage, similar enhancements can be found (TOF ≈ 1.4 vs. $0.8\,H_2\,s^{-1}$ at $|\eta_{half\,max}| = 814\,mV$; $j_0 \approx 5.2 \times 10^{-8}$ vs. $7.9 \times 10^{-10}\,A\,cm^{-2}$). The two-fold increase in TOF and more than 30-fold increase in j_0 indicates improved per-site activities and active site densities: positive shifts in onset potential values under given HER kinetics (i.e. same Tafel slope values) have been related to higher densities of active sites [11]. This, along with the onset potential shift, significantly surpasses the HER enhancement (ca. 70 mV at $|j_{half\,max}|$, see Fig. S2a ESI), found after S-edge site doping with Ni in $(Ni-MoS_2)_{1000}$ nanoclusters (3-fold increase in j_0 but lower TOF after doping) [57], indicating that the synergistic effect of sulfur enrichment and improved crystallinity prevails over a S-edge activation strategy on as-deposited MoS_x nanoclusters.

We finally proceeded to benchmark the performance of our $(MoS_x)_{1000}$ nanoclusters with recently-reported MoS_2-based catalysts from the literature. (Table S3 ESI) However, the ultra-low loadings utilized in this report preclude quantitative comparisons based on the HER metrics commonly cited ($|\eta|$ at $10\,mA\,cm^{-2}$ and $|j_{geom}|$ at 200 mV). It is well known that these metrics are heavily affected by the catalyst loading (for loading-dependent HER see Fig. S2b ESI) [54,78–81], catalyst layer thickness [67,82,83] and TMD morphologies [25,41,84]. Instead, we normalized all previous $|j_{geom}|$ reported values by mass activity (mA mg^{-1}), a metric widely accepted in the noble metal electrocatalysis community (see Table S3 ESI) [85,86]. The mass activities found for $(MoS_x)_{1000}$ nanoclusters at $|\eta|$ values as low as 400 mV (close to the HER onset) are, after sulfur evaporation and annealing, comparable with the best reported MoS_2 catalysts at 200 mV tested using a high proton concentration electrolyte. The values obtained are ca. 110 mA mg^{-1} at 5% coverage and ca. 70 mA mg^{-1} at 20% coverage (see Table S1 ESI). For $|\eta_{half\,max}|$, mass activities are in the 1000 mA mg^{-1} range: for 5% coverage, ca. 3620 mA mg^{-1} (pristine) and ca. 4010 mA mg^{-1} (sulfurised); for 20% coverage, ca. 980 mA mg^{-1} (pristine) and ca. 1040 mA mg^{-1} (sulfurised). This highlights the remarkable activities of the sulfurised $(MoS_x)_{1000}$ nanoclusters obtained at very low loadings.

The electrochemical stability of MoS_x electrocatalyts is also an important feature for evaluating prospective long-term HER performance. A preliminary comparison of the very first cathodic HER cycle recorded during our preconditioning step with the final pseudo-stationary LSV reported (11th real HER cycle, as shown in Fig. 4a and b) reveals clear differences in stability before and after sulfur evaporation and enrichment (Fig. S3 ESI). For 20% surface coverage, as-deposited and S-defficient $(MoS_x)_{1000}$ nanoclusters present an extraordinarily high activity on their first cathodic polarization scan ($|\eta_{half\,max}| \approx 380\,mV$) which dramatically decays shown by a 415 mV overpotential shift at the 11th scan (Fig. S3a). This indicates that, despite of their high activity, the edge/defect-abundant nature of amorphous MoS_x nanoclusters also confers them a high electrochemical instability. Remarkably, the S-enriched crystalline $(MoS_x)_{1000}$ nanoclusters present a dramatically enhanced stability (Fig. S3b): although their initial activity is not as high as the amorphous nanocluster counterparts, $|\eta_{half\,max}|$ is modified less than 30 mV. We believe that the improved crystallinity and subsequent minor presence of dissolution-prone under-coordinated Mo sites after S-enrichment mitigates electrochemically-induced MoS_x leaching yielding higher stabilities.

4. Conclusions

In summary, the initially sulfur-deficient $(MoS_{1.9})_{1000}$ size-selected nanoclusters obtained by magnetron sputtering and gas condensation and deposited onto glassy carbon substrates have been successfully sulfur-enriched, by sequential application of sulfur evaporation and annealing, for HER applications. This treatment has been shown to induce extended crystalline order, compared with the initially amorphous nanocluster morphology, plus the incorporation of S^{2-} moieties at the $(MoS_x)_{1000}$ nanocluster surface to yield $Mo^{4+}/Mo^aO_bS_c$: S^{2-}/S_2^{2-} ratios of 1: 4.9 $\pm$ 0.1 instead of 1:1.9 $\pm$ 0.1. The annealing step is found key to reducing fully the oxygen-containing Mo species to Mo^{4+} and maximizing sulfur incorporation at the nanoclusters surface. A consistent positive shift in the HER $|\eta_{onset}|$ was found irrespective of sample loading of S-enrichened $(MoS_x)_{1000}$ nanoclusters (approximately 200 mV), whilst the Tafel slope remained unaffected by the sulfur treatment (ca. 145 mV dec^{-1}). The 2-fold and more than 30-fold increases in TOF and j_0 values, respectively, surpass the HER enhancements previously reported after S-edge site activation by Ni in (Ni-$MoS_2)_{1000}$ hybrid nanoclusters. The results illuminate the critical role played by S-enrichment and crystallinity in MoS_x nanocluster hydrogen electrocatalysis: creating higher densities of proton-acceptor S sites and lower charge transfer resistances, as well as conferring higher electrochemical stabilities. Nanocluster benchmarking by mass activity emphasizes the remarkable performance of S-rich $(MoS_x)_{1000}$ size-selected nanoclusters at the ultra-low loading level (83.78 ng cm^{-2}, 5% surface coverage): 110.5 mA mg^{-1} at 400 mV overpotential, and 4010.5 mA mg^{-1} at $|\eta_{half\,max}| = 652\,mV$. These results are comparable to the state-of-the-art MoS_2-based catalysts, reflecting the significant activities of size-selected MoS_x nanoclusters obtained at ultra-low loadings, resembling previous enhancements reported for noble metals [87–89].

Appendix A. Supplementary data

Supplementary material related to this article can be found, in the online version, at doi:https://doi.org/10.1016/j.apcatb.2018.04.068.

References

[1] P.C.K. Vesborg, B. Seger, I. Chorkendorff, Recent development in hydrogen evolution reaction catalysts and their practical implementation, J. Phys. Chem. Lett. 6 (2015) 951–957.

[2] J.A. Turner, Sustainable hydrogen production, Science 305 (2004) 972–974.

[3] I. Roger, M.A. Shipman, M.D. Symes, Earth-abundant catalysts for electrochemical and photoelectrochemical water splitting, Nat. Rev. Chem. 1 (2017) 0003.

[4] J.D. Benck, T.R. Hellstern, J. Kibsgaard, P. Chakthranont, T.F. Jaramillo, Catalyzing the hydrogen evolution reaction (HER) with molybdenum sulfide nanomaterials, ACS Catal. 4 (2014) 3957–3971.

[5] B. Hinnemann, P. Moses, J. Bonde, K.P. Jørgensen, J.H. Nielsen, S. Horch, et al., Biomimetic hydrogen evolution: MoS$_2$ nanoparticles as catalyst for hydrogen evolution, J. Am. Chem. Soc. 127 (2005) 5308–5309.

[6] T.F. Jaramillo, K.P. Jørgensen, J. Bonde, J.H. Nielsen, S. Horch, I. Chorkendorff, Identification of active edge sites for electrochemical H$_2$ evolution from MoS$_2$ nanocatalysts, Science 317 (2007) 100–103.

[7] J. Bonde, P.G. Moses, T.F. Jaramillo, J. Norskov, I. Chorkendorff, Hydrogen evolution on nano-particulate transition metal sulfides, Faraday Discuss. 140 (2008) 219–231.

[8] M. Velický, M.A. Bissett, P.S. Toth, H.V. Patten, S.D. Worrall, A.N.J. Rodgers, et al., Electron transfer kinetics on natural crystals of MoS$_2$ and graphite, Phys. Chem. Chem. Phys. 17 (2015) 17844–17853.

[9] C.L. Bentley, M. Kang, F. Maddar, F. Li, M. Walker, J. Zhang, et al., Electrochemical maps and movies of the hydrogen evolution reaction on natural crystals of molybdenite (MoS$_2$): basal vs. edge plane activity, Chem. Sci. 8 (2017) 6583–6593.

[10] D. Voiry, J. Yang, M. Chhowalla, Recent strategies for improving the catalytic activity of 2D TMD nanosheets toward the hydrogen evolution reaction, Adv. Mater. (2016) 6197–6206.

[11] D. Voiry, M. Salehi, R. Silva, T. Fujita, M. Chen, Conducting MoS$_2$ nanosheets as catalysts for hydrogen evolution reaction, Nano Lett. 13 (2013) 6222–6227.

[12] A. Ambrosi, Z. Sofer, M. Pumera, 2H → 1T phase transition and hydrogen evolution activity of MoS$_2$, MoSe$_2$, WS$_2$ and WSe$_2$ strongly depends on the MX$_2$ composition, Chem. Commun. 51 (2015) 8450–8453.

[13] M.A. Lukowski, A.S. Daniel, F. Meng, A. Forticaux, L. Li, S. Jin, Enhanced hydrogen evolution catalysis from enhanced hydrogen evolution catalysis from chemically exfoliated metallic MoS$_2$ nanosheets, J. Am. Chem. Soc. 135 (2013) 10274.

[14] S. Bhattacharyya, T. Pandey, A.K. Singh, Effect of strain on electronic and thermoelectric properties of few layers to bulk MoS$_2$, Nanotechnology 25 (2014) 465701.

[15] D. Voiry, H. Yamaguchi, J. Li, R. Silva, D.C.B. Alves, T. Fujita, et al., Enhanced catalytic activity in strained chemically exfoliated WS$_2$ nanosheets for hydrogen evolution, Nat. Mater. 12 (2013) 850–855.

[16] K. Qi, S. Yu, Q. Wang, W. Zhang, J. Fan, W.T. Zheng, et al., Decoration of the inert basal plane of defect-rich MoS$_2$ with Pd atoms for achieving Pt-similar HER activity, J. Mater. Chem. A 4 (2016) 4025–4031.

[17] W. Xiao, P. Liu, J. Zhang, W. Song, Y.P. Feng, D. Gao, et al., Dual-functional N dopants in edges and basal plane of MoS$_2$ nanosheets toward efficient and durable hydrogen evolution, Adv. Energy Mater. 7 (2017).

[18] D. Sarkar, X. Xie, J. Kang, H. Zhang, W. Liu, J. Navarrete, et al., Functionalization of transition metal dichalcogenides with metallic nanoparticles: implications for doping and gas-sensing, Nano Lett. 15 (2015) 2852–2862.

[19] J. Deng, H. Li, J. Xiao, Y. Tu, D. Deng, H. Yang, et al., Triggering the electrocatalytic hydrogen evolution activity of the inert two-dimensional MoS$_2$ surface via single-atom metal doping, Energy Environ. Sci. 8 (2015) 1594–1601.

[20] J. Li, J. Kang, Q. Cai, W. Hong, C. Jian, W. Liu, et al., Boosting hydrogen evolution performance of MoS$_2$ by band structure engineering, Adv. Mater. Interfaces 4 (2017) 1–7.

[21] P. Liu, J. Zhu, J. Zhang, P. Xi, K. Tao, D. Gao, et al., P dopants triggered new basal plane active sites and enlarged interlayer spacing in MoS$_2$ nanosheets toward electrocatalytic hydrogen evolution, ACS Energy Lett. 2 (2017) 745–752.

[22] X. Ren, Q. Ma, H. Fan, L. Pang, Y. Zhang, Y. Yao, et al., A Se-doped MoS$_2$ nanosheet for improved hydrogen evolution reaction, Chem. Commun. 51 (2015) 15997–16000.

[23] J. Xie, H. Zhang, S. Li, R. Wang, X. Sun, M. Zhou, et al., Defect-rich MoS$_2$ ultrathin nanosheets with additional active edge sites for enhanced electrocatalytic hydrogen evolution, Adv. Mater. 25 (2013) 5807–5813.

[24] G. Ye, Y. Gong, J. Lin, B. Li, Y. He, S.T. Pantelides, et al., Defects engineered monolayer MoS$_2$ for improved hydrogen evolution reaction, Nano Lett. 16 (2016) 1097–1103.

[25] J. Xie, J. Zhang, S. Li, F. Grote, X. Zhang, H. Zhang, et al., Controllable disorder engineering in oxygen-incorporated MoS$_2$ ultrathin nanosheets for efficient hydrogen evolution, J. Am. Chem. Soc. 135 (2013) 17881–17888.

[26] Y. Ouyang, C. Ling, Q. Chen, Z. Wang, L. Shi, J. Wang, Activating inert basal planes of MoS$_2$ for hydrogen evolution reaction through the formation of different intrinsic defects, Chem. Mater. 28 (2016) 4390–4396.

[27] J. Xie, H. Qu, J. Xin, X. Zhang, G. Cui, X. Zhang, et al., Defect-rich MoS$_2$ nanowall catalyst for efficient hydrogen evolution reaction, Nano Res. 10 (2017) 1178–1188.

[28] H. Huang, L. Chen, C. Liu, X. Liu, S. Fang, W. Liu, et al., Hierarchically nanostructured MoS$_2$ with rich in-plane edges as a high-performance electrocatalyst for hydrogen evolution reaction, J. Mater. Chem. A 4 (2016) 14577–14585.

[29] Y. Kim, D.H.K. Jackson, D. Lee, M. Choi, T.W. Kim, S.Y. Jeong, et al., In situ electrochemical activation of atomic layer deposition coated MoS$_2$ basal planes for efficient hydrogen evolution reaction, Adv. Funct. Mater. 27 (2017) 1–10.

[30] D. Escalera-López, R. Griffin, M. Isaacs, K. Wilson, R.E. Palmer, N.V. Rees, MoS$_2$ and

[31] C.C. Cheng, A.Y. Lu, C.C. Tseng, X. Yang, M.N. Hedhili, M.C. Chen, et al., Activating basal-plane catalytic activity of two-dimensional MoS$_2$ monolayer with remote hydrogen plasma, Nano Energy 30 (2016) 846–852.

[32] H. Li, C. Tsai, A.L. Koh, L. Cai, A.W. Contryman, A.H. Fragapane, et al., Activating and optimizing MoS$_2$ basal planes for hydrogen evolution through the formation of strained sulphur vacancies, Nat. Mater. 15 (2015) 48–53.

[33] H. Li, M. Du, M.J. Mleczko, A.L. Koh, Y. Nishi, E. Pop, et al., Kinetic study of hydrogen evolution reaction over strained MoS$_2$ with sulfur vacancies using scanning electrochemical microscopy, J. Am. Chem. Soc. 138 (2016) 5123–5129.

[34] Y. Yin, J. Han, Y. Zhang, X. Zhang, P. Xu, Q. Yuan, et al., Contributions of phase, sulfur vacancies, and edges to the hydrogen evolution reaction catalytic activity of porous molybdenum disulfide nanosheets, J. Am. Chem. Soc. 138 (2016) 7965–7972.

[35] C. Tsai, H. Li, S. Park, J. Park, H.S. Han, J.K. Nørskov, et al., Electrochemical generation of sulfur vacancies in the basal plane of MoS$_2$ for hydrogen evolution, Nat. Commun. 8 (2017) 15113.

[36] L. Lin, N. Miao, Y. Wen, S. Zhang, P. Ghosez, Z. Sun, et al., Sulfur-depleted monolayered molybdenum disulfide nanocrystals for superelectrochemical hydrogen evolution reaction, ACS Nano. 10 (2016) 8929–8937.

[37] Y. Deng, L.R.L. Ting, P.H.L. Neo, Y.-J. Zhang, A.A. Peterson, B.S. Yeo, Operando raman spectroscopy of amorphous molybdenum sulfide (MoS$_x$) during the electrochemical hydrogen evolution reaction: identification of sulfur atoms as catalytically active sites for H$^+$ reduction, ACS Catal. (2016) 7790–7798.

[38] Y. Guo, X. Zhang, X. Zhang, T. You, Defect- and S-rich ultrathin MoS$_2$ nanosheet embedded N-doped carbon nanofibers for efficient hydrogen evolution, J. Mater. Chem. A 3 (2015) 15927–15934.

[39] H. Zhu, M. Du, M. Zhang, M. Zou, T. Yang, S. Wang, et al., S-rich single-layered MoS$_2$ nanoplates embedded in N-doped carbon nanofibers: efficient co-electrocatalysts for the hydrogen evolution reaction, Chem. Commun. 50 (2014) 15435–15438.

[40] P.D. Tran, T.V. Tran, M. Orio, S. Torelli, Q.D. Truong, K. Nayuki, et al., Coordination polymer structure and revisited hydrogen evolution catalytic mechanism for amorphous molybdenum sulfide, Nat. Mater. 15 (2016) 1–8.

[41] Y. Li, Y. Yu, Y. Huang, R.A. Nielsen, W.A. Goddard, Y. Li, et al., Engineering the composition and crystallinity of molybdenum sulfide for high-performance electrocatalytic hydrogen evolution, ACS Catal. 5 (2015) 448–455.

[42] M.J. Cuddy, K.P. Arkill, Z.W. Wang, H.-P. Komsa, A.V. Krasheninnikov, R.E. Palmer, Fabrication and atomic structure of size-selected, layered MoS$_2$ clusters for catalysis, Nanoscale 6 (2014) 12463–12469.

[43] Y. Niu, S. Park, R. Palmer, Modification of deposited, size-selected MoS$_2$ nanoclusters by Sulphur addition: an aberration-corrected STEM study, Inorganics 5 (2016) 1.

[44] S. Pratontep, S.J. Carroll, C. Xirouchaki, M. Streun, R.E. Palmer, Size-selected cluster beam source based on radio frequency magnetron plasma sputtering and gas condensation, Rev. Sci. Instrum. 76 (2005) 045103.

[45] B. von Issendorff, R.E. Palmer, A new high transmission infinite range mass selector for cluster and nanoparticle beams, Rev. Sci. Instrum. 70 (1999) 4497.

[46] Z.W. Wang, O. Toikkanen, F. Yin, Z.Y. Li, B.M. Quinn, R.E. Palmer, Counting the atoms in supported, monolayer-protected gold clusters, J. Am. Chem. Soc. 132 (2010) 2854–2855.

[47] N. Jian, C. Stapelfeldt, K.-J. Hu, M. Fröba, R.E. Palmer, Hybrid atomic structure of the schmid cluster Au$_{55}$(PPh$_3$)$_{12}$Cl$_6$ resolved by aberration-corrected STEM, Nanoscale 7 (2015) 885–888.

[48] E.J.F. Dickinson, J.G. Limon-Petersen, N.V. Rees, R.G. Compton, How Much supporting electrolyte is required to make a cyclic voltammetry experiment quantitatively "diffusional"? A theoretical and experimental investigation, J. Phys. Chem. C. 113 (2009) 11157–11171.

[49] Z. Wu, Y. Wang, Y. Ye, J. Feng, M. Zhang, Y. Luo, et al., First-principles study of monolayer MoS$_2$ with deficient and excessive Mon and Sn (n = -3→3) clusters on 5 x 5 supercells, Comput. Mater. Sci. 121 (2016) 124–130.

[50] R.P. Tucker, Notes on the sublimation of sulfur between 25° and 50° C, Ind. Eng. Chem. 21 (1929) 44–47.

[51] R.N. Grugel, H. Toutanji, Sulfur "concrete" for lunar applications – sublimation concerns, Adv. Sp. Res. 41 (2008) 103–112.

[52] E. Schmidt, C. Sourisseau, G. Meunier, A. Levasseur, Amorphous molybdenum oxysulfide thin films and their physical characterization, Thin Solid Films 260 (1995) 21–25.

[53] W. Grunert, A.Y. Stakheev, R. Feldhaus, K. Anders, E.S. Shpiro, K.M. Minachev, analysis of Mo(3d) XPS spectra of supported Mo catalysts: an alternative approach, J. Phys. Chem. 95 (1991) 1323–1328.

[54] H. Vrubel, X. Hu, Growth and activation of an amorphous molybdenum sulfide hydrogen evolving catalyst, ACS Catal. 3 (2013) 2002–2011.

[55] T. Weber, J.C. Muijsers, J.W. Niemantsverdriet, Structure of amorphous MoS$_3$, J. Phys. Chem. 99 (1995) 9194–9200.

[56] S.R. Kelemen, G.N. George, M.L. Gorbaty, Direct determination and quantification of sulphur forms in heavy petroleum and coals 1. The X-ray photoelectron spectroscopy (XPS) approach, Fuel 69 (1990) 939–944.

[57] D. Escalera-López, Y. Niu, J. Yin, K. Cooke, N.V. Rees, R.E. Palmer, Enhancement of the hydrogen evolution reaction from Ni-MoS$_2$ hybrid nanoclusters, ACS Catal. (2016) 6008–6017.

[58] C.E. Blackmore, N.V. Rees, R.E. Palmer, Modular construction of size-selected multiple-core Pt-TiO$_2$ nanoclusters for electro-catalysis, Phys. Chem. Chem. Phys. (2015).

[59] Y. Zheng, Y. Jiao, M. Jaronice, S.Z. Qiao, Advancing the electrochemistry of the

hydrogen-evolution reaction through combining experiment and theory, Angew. Chem. Int. Ed. Engl. 54 (2015) 52–65.

[60] N. Dubouis, C. Yang, R. Beer, L. Ries, D. Voiry, A. Grimaud, Interfacial interactions as an electrochemical tool to understand Mo-based catalysts for the hydrogen evolution reaction, ACS Catal. 8 (2017) 828–836.

[61] T.R. Hellstern, J. Kibsgaard, C. Tsai, D.W. Palm, L.A. King, F. Abild-Pedersen, et al., Investigating catalyst–support interactions to improve the hydrogen evolution reaction activity of thiomolybdate $[Mo_3S_{13}]^{2-}$ nanoclusters, ACS Catal. (2017) 7126–7130.

[62] J. Kibsgaard, T.F. Jaramillo, F. Besenbacher, Building an appropriate active-site motif into a hydrogen-evolution catalyst with thiomolybdate $[Mo_3S_{13}]^{2-}$ clusters, Nat. Chem. 6 (2014) 248–253.

[63] J. Bisquert, G. Garcia-Belmonte, F. Fabregat-Santiago, A. Compte, Anomalous transport effects in the impedance of porous film electrodes, Electrochem. Commun. 1 (1999) 429–435.

[64] J. Bisquert, G. Garcia-Belmonte, F. Fabregat-Santiago, N.S. Ferriols, P. Bogdanoff, E.C. Pereira, Doubling exponent models for the analysis of porous film electrodes by impedance. Relaxation of TiO_2 nanoporous in aqueous solution, J. Phys. Chem. B 104 (2000) 2287–2298.

[65] A.P. Murthy, J. Theerthagiri, J. Madhavan, K. Murugan, Highly active MoS_2/carbon electrocatalysts for the hydrogen evolution reaction – insight into the effect of the internal resistance and roughness factor on the Tafel slope, Phys. Chem. Chem. Phys. 19 (2017) 1988–1998.

[66] H. Vrubel, T. Moehl, M. Grätzel, X. Hu, Revealing and accelerating slow electron transport in amorphous molybdenum sulphide particles for hydrogen evolution reaction, Chem. Commun. 49 (2013) 8985.

[67] Y. Yu, S.Y. Huang, Y. Li, S.N. Steinmann, W. Yang, L. Cao, Layer-dependent electrocatalysis of MoS_2 for hydrogen evolution, Nano Lett. 14 (2014) 553–558.

[68] D. Fu, J. Zhou, S. Tongay, K. Liu, W. Fan, T.J. King Liu, et al., Mechanically modulated tunneling resistance in monolayer MoS_2, Appl. Phys. Lett. 103 (2013) 32–35.

[69] R. M, S.a Salam, Electrical properties of molybdenite, Proc. Phys. Soc. Sect. B. 66 (1953) 377.

[70] S.R.G. Thakurta, Electrical properties of molybdenite, Indian J. Phys. 43 (1969) 169–172.

[71] H. Tributsch, J.C. Bennett, Electrochemistry and photochemistry of MoS_2 layer crystals. I, J. Electroanal. Chem. 81 (1977) 97–111.

[72] L.R.L. Ting, Y. Deng, L. Ma, Y.J. Zhang, A.A. Peterson, B.S. Yeo, Catalytic activities of sulfur atoms in amorphous molybdenum sulfide for the electrochemical hydrogen evolution reaction, ACS Catal. 6 (2016) 861–867.

[73] J.D. Benck, Z. Chen, L.Y. Kuritzky, A.J. Forman, T.F. Jaramillo, Amorphous molybdenum sulfide catalysts for electrochemical hydrogen production: insights into the origin of their catalytic activity, ACS Catal. 2 (2012) 1916–1923.

[74] M.A. Baker, R. Gilmore, C. Lenardi, W. Gissler, XPS investigation of preferential sputtering of S from MoS_2 and determination of MoS_x stoichiometry from Mo and S peak positions, Appl. Surf. Sci. 150 (1999) 255–262.

[75] J.S. Kim, J. Kim, J. Zhao, S. Kim, J.H. Lee, Y. Jin, et al., Electrical transport properties of polymorphic MoS_2, ACS Nano. 10 (2016) 7500–7506.

[76] B. Lassalle-Kaiser, D. Merki, H. Vrubel, S. Gul, V.K. Yachandra, X. Hu, et al., Evidence from in situ X-ray absorption spectroscopy for the involvement of terminal disulfide in the reduction of protons by an amorphous molybdenum sulfide electrocatalyst, J. Am. Chem. Soc. 137 (2015) 314–321.

[77] D. Escalera-López, R. Griffin, M. Isaacs, K. Wilson, R.E. Palmer, N.V. Rees, Electrochemical sulfidation of WS_2 nanoarrays: strong dependence of hydrogen evolution activity on transition metal sulfide surface composition, Electrochem. Commun. 81 (2017) 106–111.

[78] M.-R. Gao, M.K.Y. Chan, Y. Sun, Edge-terminated molybdenum disulfide with a 9.4-Å interlayer spacing for electrochemical hydrogen production, Nat. Commun. 6 (2015) 7493.

[79] J. Kibsgaard, Z. Chen, B.N. Reinecke, T.F. Jaramillo, Engineering the surface structure of MoS_2 to preferentially expose active edge sites for electrocatalysis, Nat. Mater. 11 (2012) 963–969.

[80] J. Kibsgaard, T.F. Jaramillo, Molybdenum phosphosulfide: an active, acid-stable, earth-abundant catalyst for the hydrogen evolution reaction, Angew. Chem. Int. Ed. Engl. 53 (2014) 14433–14437.

[81] Y. Zhang, L. Zuo, Y. Huang, L. Zhang, F. Lai, W. Fan, et al., In-situ growth of few-layered MoS_2 nanosheets on highly porous carbon aerogel as advanced electrocatalysts for hydrogen evolution reaction, ACS Sustain. Chem. Eng. 3 (2015) 3140–3148.

[82] D. McAteer, Z. Gholamvand, N. McEvoy, A. Harvey, E. O'Malley, G.S. Duesberg, et al., Thickness dependence and percolation scaling of hydrogen production rate in MoS_2 nanosheet and nanosheet–carbon nanotube composite catalytic electrodes, ACS Nano 10 (2016) 672–683.

[83] B. Seo, G.Y. Jung, Y.J. Sa, H.Y. Jeong, J.Y. Cheon, J.H. Lee, et al., Monolayer-precision synthesis of molybdenum sulfide nanoparticles and their nanoscale size effects in the hydrogen evolution reaction, ACS Nano. 9 (2015) 3728–3739.

[84] G. Li, D. Zhang, Q. Qiao, Y. Yu, D. Peterson, A. Zafar, et al., All the catalytic active sites of MoS_2 for hydrogen evolution, J. Am. Chem. Soc. 138 (2016) 16632–16638.

[85] Y. Garsany, J. Ge, J. St-Pierre, R. Rocheleau, K.E. Swider-Lyons, Analytical procedure for accurate comparison of rotating disk electrode results for the oxygen reduction activity of Pt/C, J. Electrochem. Soc. 161 (2014) F628–F640.

[86] K.J.J. Mayrhofer, D. Strmcnik, B.B. Blizanac, V. Stamenkovic, M. Arenz, N.M. Markovic, Measurement of oxygen reduction activities via the rotating disc electrode method: from Pt model surfaces to carbon-supported high surface area catalysts, Electrochim. Acta 53 (2008) 3181–3188.

[87] E.A. Paoli, F. Masini, R. Frydendal, D. Deiana, C. Schlaup, M. Malizia, et al., Oxygen evolution on well-characterized mass-selected Ru and RuO_2 nanoparticles, Chem. Sci. 6 (2015) 190–196.

[88] E. Kemppainen, A. Bodin, B. Sebok, T. Pedersen, B. Seger, B. Mei, et al., Scalability and feasibility of photoelectrochemical H_2 evolution: the ultimate limit of Pt nanoparticle as an HER catalyst, Energy Environ. Sci. 8 (2015) 2991–2999.

[89] P. Hernandez-Fernandez, F. Masini, D.N. McCarthy, C.E. Strebel, D. Friebel, D. Deiana, et al., Mass-selected nanoparticles of Pt_xY as model catalysts for oxygen electroreduction, Nat. Chem. 6 (2014) 732–738.